

See discussions, stats, and author profiles for this publication at: <https://www.researchgate.net/publication/223975682>

Ultra-Subwavelength Two-Dimensional Plasmonic Circuits

ARTICLE *in* NANO LETTERS · APRIL 2012

Impact Factor: 13.59 · DOI: 10.1021/nl300046g · Source: PubMed

CITATIONS

25

READS

70

7 AUTHORS, INCLUDING:



Kitty Y M Yeung

Harvard University

8 PUBLICATIONS 73 CITATIONS

SEE PROFILE

Ultra-Subwavelength Two-Dimensional Plasmonic Circuits

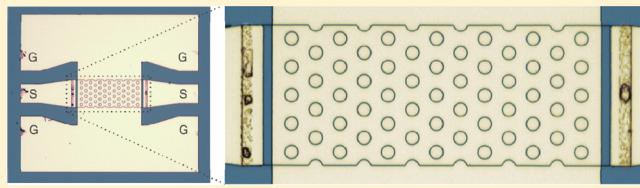
William F. Andress,[†] Hosang Yoon,[†] Kitty Y. M. Yeung,[†] Ling Qin,[†] Ken West,[‡] Loren Pfeiffer,[‡] and Donhee Ham^{*†}

[†]School of Engineering and Applied Sciences, Harvard University, 33 Oxford Street, Cambridge, Massachusetts 02138, United States

[‡]Department of Electrical Engineering, Princeton University, Princeton, New Jersey 08544, United States

Supporting Information

ABSTRACT: We report electronics regime (GHz) two-dimensional (2D) plasmonic circuits, which locally and nonresonantly interface with electronics, and thus offer to electronics the benefits of their ultrasubwavelength confinement, with up to 440,000-fold mode-area reduction. By shaping the geometry of 2D plasmonic media 80 nm beneath an unpatterned metallic gate, plasmons are routed freely into various types of reflections and interferences, leading to a range of plasmonic circuits, e.g., plasmonic crystals and plasmonic-electromagnetic interferometers, offering new avenues for electronics.



KEYWORDS: Plasmonics, two-dimensional electron gas, plasmonic circuits, plasmonic crystals, photonic crystals, microwaves

When the electron density distribution in solid-state conductors is perturbed from equilibrium, Coulomb restoring forces arise and power collective electron density waves. In these plasmonic waves, electrons accelerate and decelerate collectively; their corresponding time-varying kinetic energy serves as a defining energetic component of the plasmonic waves, and is largely responsible for the plasmons' behavioral divergence from light waves, such as the reduced plasmonic velocity. A notable example of the solid-state plasmonic wave is the surface plasmons on bulk three-dimensional (3D) metals, which have been a source of many breakthroughs in optics.^{1–11}

While surface plasmons are particularly well-suited to the optics regime, plasmonic waves in 2D conductors, such as GaAs/AlGaAs heterostructures, where electrons are perfectly confined into two dimensions, can emerge at much lower frequencies down to the gigahertz (GHz) range, falling into the regime of electronics. This difference lies in how the wave energetics is fundamentally modified by the reduced dimensionality. On the surface of a 3D metal, where electrons do not have such 2D confinement, an electromagnetic wave traveling along the surface gives rise to currents that are contained within a certain penetration depth.¹² At frequencies below the optics regime, the penetration depth is thick enough to contain a very large number of electrons, which can produce these surface currents without accelerating to high velocities. Accordingly, the total kinetic energy of electrons in the collective plasma mode is unappreciable compared to the energy of the surrounding electromagnetic fields.¹³ Hence it is difficult to observe surface plasmons below the optics regime with 3D metals. By contrast, in two dimensions, all of the conducting electrons, which are smaller in number, participate in the current regardless of frequency. Therefore, the total kinetic energy of electrons associated with a given current in a

2D conductor is substantial and independent of frequency, enabling 2D plasmonic waves at frequencies far below the optics regime. Indeed, since their first observations at far-infrared in 1977,¹⁴ 2D plasma waves have been shown to emerge at frequencies as low as the GHz range.^{15–17} These low-frequency 2D plasma waves can be obscured by damping if the long period of oscillation is not accommodated by the electron scattering time. Particular 2D electron systems, such as GaAs/AlGaAs junctions at cryogenic temperature, boast exceptionally long electron scattering times. In these systems, electrons may oscillate several times even at GHz frequencies before scattering.

Another unique property of 2D plasmons is their velocity v_p , that can be far lower^{17–19} than what is observed in surface plasmons, typically limited to around^{4,7–9} $c/10$ (c : free-space speed of light). In our work, v_p is as small as $c/660$ (see Supporting Information). The underlying physics of this extreme wave slowing, or extreme wavelength reduction, is two-fold. First, the aforementioned significant kinetic character of 2D plasmons due to the reduced dimensionality substantially lowers v_p . From the circuit point of view, this substantial kinetic character corresponds to an exceedingly large kinetic inductance per square,¹⁷ which can be 3~4 orders of magnitude larger than magnetic inductance per square. While surface plasmons achieve substantial kinetic character as the excitation frequency increases toward the surface plasmon resonance frequency (of theoretically infinite wavenumber), loss ultimately prevents surface plasmons from approaching such extreme limits. Second, a top gate placed close to the 2D plasmonic medium screens the Coulomb restoring force that

Received: January 4, 2012

Revised: March 26, 2012

Published: April 11, 2012



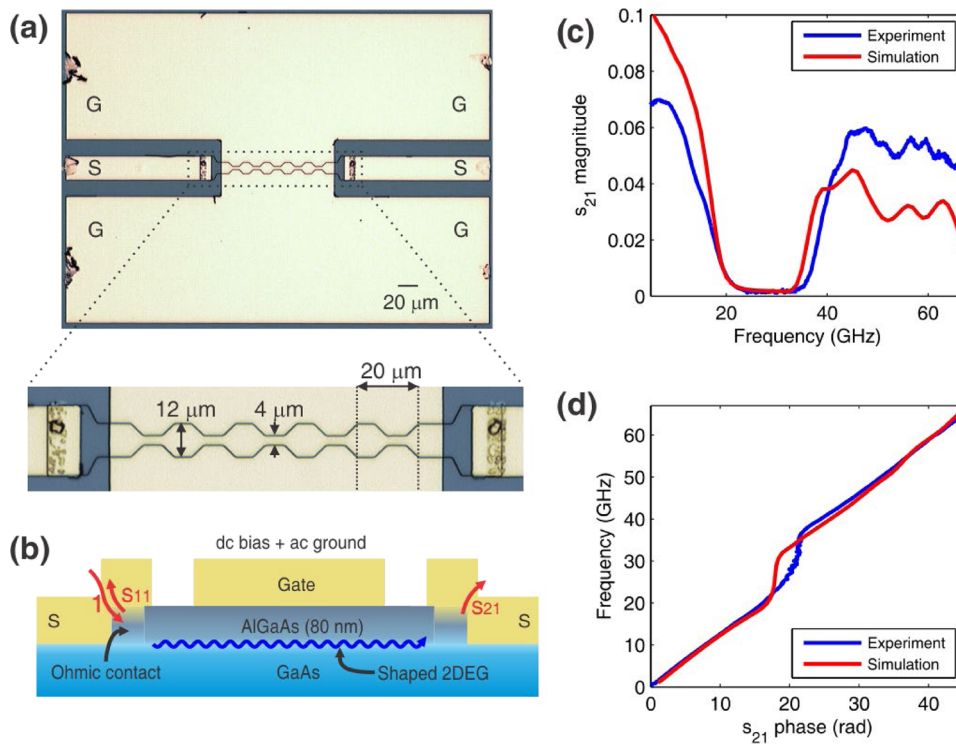


Figure 1. (a) Optical image of plasmonic crystal structure. CPWs (signal line ‘S’ and ground lines ‘G’) that direct electromagnetic waves to and from the device are also shown. (b) Diagram showing the cross section of the device. Electromagnetic waves (red curves) couple to plasmonic waves (blue curve), which propagate underneath the gate through the periodically shaped 2DEG. (c) Measured (blue) and simulated (red) transmission (s_{21}) magnitude through the device at 0.5 V bias, showing plasmonic bandgap from 24 to 34 GHz. (d) Measured (blue) and simulated (red) s_{21} phase curve (plasmon dispersion diagram). Note that in part (d), the frequency is plotted on the y-axis, following the convention for dispersion diagrams (ω vs k).

causes the collective electron accelerations,²⁰ further reducing v_p .

Here we report electronics regime (GHz) passive plasmonic circuits, which offer the benefits of 2D plasmons’ ultra-subwavelength confinement to electronics, as they can operate in direct interface with electronics. To this end we first construct 2D plasmonic waveguides consisting of a highly degenerate GaAs/AlGaAs 2D electron gas (2DEG) at 3 K as a 2D plasmonic medium and a metallic top gate 80 nm above the 2DEG as a ‘plasmonic ground’, thus creating localized input and output terminals. Through these local terminals, the plasmonic waveguide can be directly and nonresonantly excited over a continuous frequency range (as opposed to a discrete set of coupling frequencies), driven by the voltage and current of an electromagnetic signal (thus electronics) guided to a local terminal. This direct local coupling of electromagnetic signals to the full spectrum of plasmons allows the full freedom to route and manipulate plasmons in between these local terminals. This manipulation is done by freely shaping the planar geometry of 2DEG, the plasmonic signal medium itself, within the plasmonic waveguide. Plasmons are routed according to designer geometries to undergo various reflections and interferences, leading to GHz plasmonic circuits (Figures 1–4) with a range of functionalities, such as plasmonic-electromagnetic interferometers, plasmonic cavities, and plasmonic bandgap crystals with designer bandgap characteristics (controllable numbers and positions) and with 1D and 2D periodicities. These plasmonic circuits achieve extreme subwavelength confinement due to the large 2D kinetic inductance and the top gate, or plasmonic ground, which

shortens the Coulomb interaction range of electrons, occupying areas up to $\sim 440\,000$ times smaller than their electromagnetic counterparts, which are ubiquitous in electronics but not subject to Moore’s law scaling enjoyed by transistors.

Prior experimental works include various interesting passive 2D plasmonic devices,^{14–18,23} whose operation ranges from GHz to THz to far-infrared. One novel feature of our approach is the use of geometric shaping of the plasmonic medium to route plasmons between local ports, whereas previous works have mostly employed an overall exposure of the 2D plasma to electromagnetic waves, with the absorption occurring at some discrete set of resonant coupling frequencies. This resonant coupling arises from the periodicity of grating couplers above the plasma,^{14,18,23} or from the plasma’s spatial confinement;^{15–17} one example of the latter type involves GHz electromagnetic signals delivered to a gate metal overlying a bounded plasma, maximally absorbed at the plasma resonances.¹⁷ A different, active, type of 2D plasmonic devices attain THz emission via instability-mediated 2D plasma oscillation;^{19,24} as devices in this regime have yet to utilize the shaping of the plasmonic medium, it would thus be an interesting possibility to combine our passive shaping principle with these active mechanisms.

A starting example of our approach is the plasmonic bandgap crystal (Figure 1a). Here the plasmonic waveguide consists of the 2DEG as a plasmonic signal medium and a top gate metal 80-nm above (Figures 1a,b), where the gate will act as a ‘plasmonic ground’ if configured properly (see below). The planar geometry of the 2DEG is physically shaped by mesa etching into a channel of periodically varying width, while the

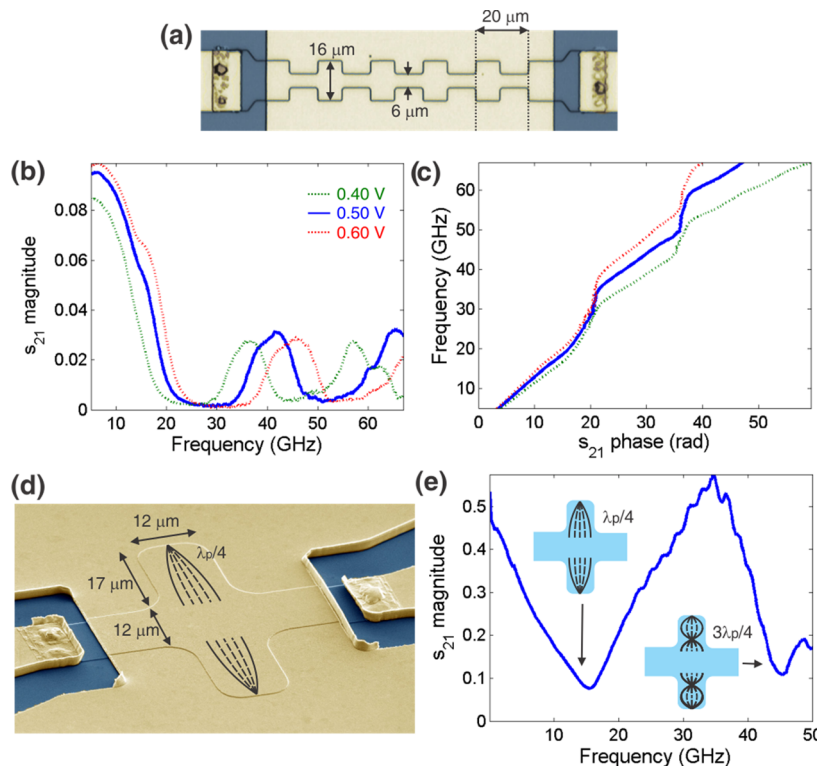


Figure 2. (a) Optical image of a periodic array of cavities. (b) s_{21} magnitude curves of the device in (a) at different bias voltages. (c) s_{21} phase curves (plasmon dispersion diagrams) of the device in (a). Different slopes at each bias voltage reflect different plasma wave velocities. (d) Scanning electron micrograph of a stand-alone plasmonic cavity circuit (false colored). The current amplitude profile of a $\lambda_p/4$ standing wave resonance in each vertical stub is illustrated. (e) Measured transmission (s_{21}) magnitude through the device at 0.5 V bias, with the effects of ohmic contacts de-embedded. The two resonance modes are illustrated.

gate is not patterned. The plasmonic waveguide is excited at either of the local terminals on the left and right, each of which connects the shaped 2DEG to the signal line (labeled “S”, Figures 1a-b) of a purely electromagnetic on-chip metallic coplanar waveguide (CPW), via a Ni/Au/Ge ohmic contact. Each CPW, deposited over the etched insulating region, consists of the signal line and two ground lines (labeled “G”, Figure 1a). The CPWs’ ground lines connect with the gate, allowing this gate to act as a plasmonic ground. This ground sharing prevents the gate itself from becoming a signal path, such that a purely plasmonic waveguide continues from the purely electromagnetic CPWs (see Supporting Information); this is an important principle to make our plasmonic circuits work, and is different from works that use a gate as an overall excitation source of the underlying plasma.¹⁷

When the plasmonic crystal (Figure 1a) is excited at the left terminal, a plasmonic wave is launched rightward. Transmission through the crystal is measured as the microwave scattering parameter s_{21} at the right terminal up to 66 GHz (see Supporting Information). Due to the crystal periodicity, a bandgap (24–34 GHz) occurs in the measurement (Figure 1c). This bandgap arises from the first Brillouin-zone boundary, where the 20 μm period equals half the plasmonic wavelength, $\lambda_p/2$. Since the frequency corresponding to the zone boundary must lie in this band, the plasmonic velocity v_p lies somewhere between $c/220$ and $c/310$, thus, λ_p is 265 ± 45 times smaller than the free-space electromagnetic wavelength, λ . The direct, nonresonant, interface of plasmonic circuits with electronics (measurement setup here) also makes possible direct measurement of the dispersion relation, which is simply s_{21} ’s phase (proportional to Bloch wavenumber k_p) measured over a

continuous frequency range. As expected, the plasmonic crystals’ dispersion (Figure 1d) contains a discontinuity over the bandgap. The spurious phase deviation within the bandgap arises from parasitic signals. From the dispersion curve’s passband slope, we extract $v_p \sim c/(300 \pm 30)$, with precision limited by the frequency-dependent effects of the ohmic contacts on s_{21} ’s phase (v_p is extracted more accurately later). The next bandgap does not occur until the third Brillouin-zone boundary,²⁵ beyond our measurement range. Simulated s parameters obtained using Sonnet frequency-domain field solver with estimated values of kinetic inductance and ohmic contact parameters resemble the measured s parameters (Figure 1c,d) in the overall bandgap character, with very similar bandgap positions; the differing transmission amplitudes are due to the estimated nature of the ohmic contact parameters used in the simulation. Note that within the bandgap, spurious fluctuations in the measured s_{21} phase (Figure 1d, blue curve, x-axis) arise due to the bandgap’s low signal transmission.

The plasmonic crystal serves to introduce a general geometric-shaping principle, which allows a great deal of versatility. For instance one can begin to add subtle variation to the crystal’s geometry to produce a conspicuous behavioral difference. Figure 2a shows a variation on the plasmonic crystal, where the transitions between the thin and thick sections are made abruptly. The plasmonic dynamics here cannot be simply viewed as a perturbed horizontal routing as in Figure 1; one must also consider the vertical routing of plasmons to and from the ends of the thick sections or vertical stubs (each thick section contains two symmetric stubs). These vertical stubs act as plasmonic cavities, which resonate when plasmons routed toward and reflected from the stub ends interfere to form

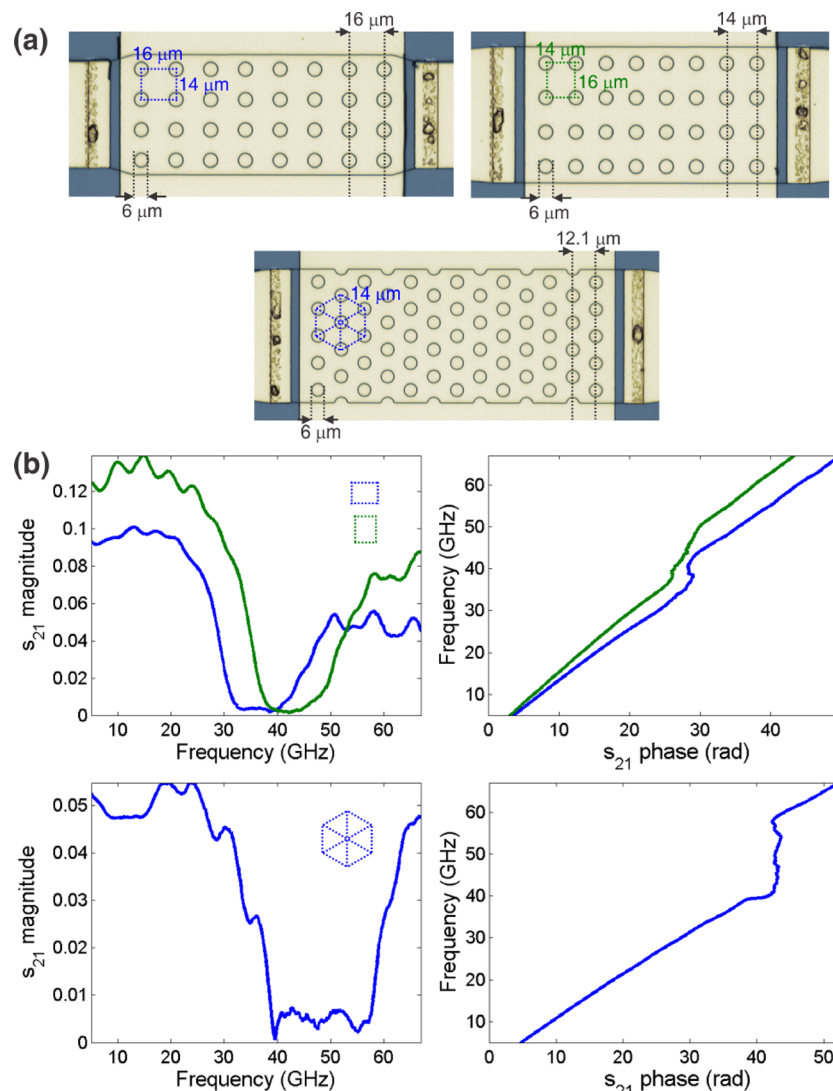


Figure 3. (a) Device images of rectangular and hexagonal 2D plasmonic crystals. (b) s_{21} magnitude (left) and s_{21} phase (right) of rectangular (top) and hexagonal (bottom) crystals at 0.5 V bias. The three devices have similar velocities; note that the phase curve's slope must be multiplied by the device length in order to extract the velocity, hence, the difference in slope between the two rectangular orientations despite their similar velocities.

standing waves. The repetition of the plasmonic cavity is expected to result in another bandgap at around the cavity resonance frequency. The measured transmission (Figure 2b,c) indeed includes not only the Brillouin-zone boundary bandgap, as in Figure 1c, but also the additional bandgap, centered about 52 GHz, from the cavity resonance.

To verify this cavity behavior, we build a stand-alone cavity structure with two vertical stubs (Figure 2d). At the frequency where the stub lengths are $\lambda_p/4$, a standing wave resonance should emerge. In this situation, the standing wave's current [voltage] amplitude is zero [maximal] at the stub ends (which act as open circuits; fringing capacitances to the gate are negligible) and maximal [zero] at the stub inlets (Figure 2d). Thus at the $\lambda_p/4$ frequency, the impedance at the inlets becomes zero, and the entire wave is absorbed into the stubs, with nothing transmitted to the right terminal. The s_{21} (Figure 2e) measured from the stand-alone cavity structure indeed shows this characteristic, with the $\lambda_p/4$ absorption at 15 GHz. Given the 17 μm stub length, this corresponds to $\lambda_p = 68 \mu\text{m} = \lambda/294$, thus $v_p = c/294$. Another standing wave resonance expected when the stub length is $3\lambda_p/4$ indeed appears at 45

GHz. The cavity may be viewed as a 'plasmon trap' with frequency-dependent potential in the particle picture. This resonance from the cross-shaping is independent of the input coupling. The more precise estimate of $v_p=c/294$ obtained from the cavity behavior is within the range deduced from the bandgap of Figure 1c and also within that deduced from the passband slope of Figure 1d. Also we can now verify that the additional bandgap (Figure 2b) from the crystal of Figure 2a originates from its vertical cavities; if we continue to assume $v_p = c/294$ (although different structures may support slightly different v_p since mesa boundaries influence electron density), the $\lambda_p/4$ resonance in the 5 μm long cavities should occur at ~51 GHz, which indeed falls within the second bandgap (Figure 2b).

The extremely slow plasmonic velocity $v_p = c/294$ (thus extremely short plasmonic wavelength $\lambda_p = \lambda/294$) drastically miniaturizes the 2D plasmonic circuits relative to their electromagnetic counterparts. As mentioned earlier, this ultra-subwavelength confinement is attained by the inherently large 2D kinetic inductance of the plasmonic medium and the top gate shortening the Coulomb interaction range of electrons in

the 2DEG. These two factors in conjunction result in $v_p \sim 4v_F$ (v_F is the Fermi velocity), for which the Coulomb restoring force is ~ 30 times stronger than the restoring force due to electron degeneracy pressure.^{20–22} Using the gate as a direct current (dc) bias, we can alter the 2DEG's electron density, thus, kinetic inductance by changing the gate's bias relative to the signal line, tuning v_p (and simultaneously, v_F , keeping $v_p \sim 4v_F$) from $c/187$ at 0.8 V to $c/660$ at -0.13 V (see Supporting Information). This tunability can be seen in Figure 2b,c, where the bandgap frequencies and dispersion slopes are altered with bias. With λ_p as small as $\lambda/660$, plasmonic circuits can occupy up to $\sim 440\,000$ times less area than their electromagnetic counterparts.

Another advantage is apparent from the quality factor, Q , at the $\lambda_p/4$ and $3\lambda_p/4$ resonances, estimated as 4.1 and 13 from their fwhm (Figure 2e). The almost linear increase of Q with frequency is characteristic of plasmons, for which $Q/2\pi$ equals frequency times momentum relaxation time τ , indicating how many times electrons oscillate between collisions with crystal impurities, defects, and vibrations. Thus while this work demonstrates prototype plasmonic circuits at 3 K to attain a long enough τ to achieve $Q \sim 10$ at GHz frequencies, their linearly increasing Q suggests an intrinsic scalability of our plasmonic circuits, based on the geometric shaping of the plasmonic medium and the resultant plasmon routing manipulation, into higher frequencies, with possible applicability toward the THz gap,²⁶ where room temperature implementation may be feasible. With the recent observation of light-plasmon coupling in graphene at THz and room temperature,²⁷ graphene may offer an especially interesting 2DEG platform on which to apply our shaping-based plasmon manipulation principle.

To illustrate our principle further, we create plasmonic crystals with 2D periodicity, by etching lattices of holes into the 2DEG. Two rectangular lattices and a hexagonal lattice are shown in Figure 3a. The two rectangular lattices have identical unit cells, but the orientation of each lattice relative to the propagation direction of the plasmonic waves differs by 90° . For plasmons traveling rightward in each lattice, a Brillouin-zone boundary bandgap occurs when the distance between adjacent vertical crystal planes is $\lambda_p/2$. Since these separations are 16, 14, and $12.1\ \mu\text{m}$ in the three lattices and the bandgap in the first structure occurs about 36 GHz ($v_p \sim c/260$), we expect bandgaps in the other two structures near 41 and 48 GHz, which indeed fall within the corresponding measured bandgaps (Figure 3b). The frequency positions of the discontinuities in the measured dispersions follow these ratios as well.

While all the above circuits exploit interferences of multiple plasma waves, another interesting avenue to explore is interference between plasmonic and purely electromagnetic waves. Figure 4 shows a hybrid electromagnetic-plasmonic interferometer. The 2DEG, excited from the left contact, is split into two smaller 2DEG branches of equal width. The gate that covers the bottom branch is connected to one of the ground lines of the metallic coplanar waveguide (CPW). Therefore, as in all previous circuits of Figures 1–3, this branch acts as a plasmonic signal path. The top branch, on the other hand, is covered by a gate that is not connected to the CPW ground. Although this gate is biased by a dc probe, at GHz frequencies the inductance of the dc probe and cable greatly impedes current from flowing through it. Therefore, this gate effectively functions as a ‘floating’ gate and becomes a path for propagation of electromagnetic waves, as opposed to plasmonic

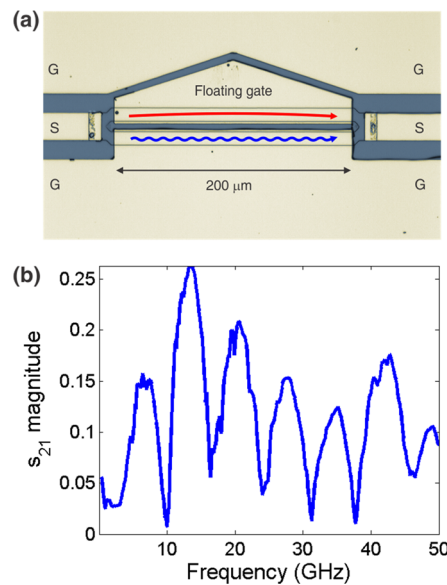


Figure 4. Hybrid electromagnetic-plasmonic interferometer. (a) Optical image. A purely electromagnetic wave (red curve) propagates along the floating gate, while a purely plasmonic wave (blue curve) propagates along the 2DEG below the grounded gate that is connected to the ground lines of the CPWs. (b) s_{21} magnitude curve of the device at 0.8 V bias. Repeated peaks and valleys result from the interference between plasmonic and electromagnetic waves.

waves (see Supporting Information for more details). The signal is therefore divided into a slow plasmonic wave in one path and a fast electromagnetic wave in the other, with amplitudes of similar magnitude. As the excitation frequency is swept up to 50 GHz, the phase of the slow plasmonic wave rapidly changes, while the phase of the fast electromagnetic wave remains nearly the same, resulting in interference. The measured interference pattern (Figure 4b) features a sequence of dips, which occur when the two types of waves interfere destructively or when the plasmonic wave's phase shift differs by an odd multiple of a half cycle relative to the nearly constant phase of the electromagnetic wave. These dips are separated by 6 GHz, implying v_p of $c/238$ in this particular structure at 0.8 V gate bias. Note that while a plasmonic Fabry–Perot resonance could manifest similarly to the measured interferometric pattern, dissipations in the ohmic contacts and 2DEG prevent it in this circuit of Figure 4 as well as all other devices found in Figures 1–3, except for a very weak Fabry–Perot resonance in the short device of Figure 2d,e (see Supporting Information).

We have presented a small set of plasmonic circuits as examples illustrating our principle of geometric-shaping based ultra-subwavelength 2D plasmon routing manipulation. The principle can be applied very generally to create a wide variety of circuits. The present work follows a similar spirit to how electromagnetic wave manipulation via structuring of electromagnetic media has created a wide variety of resonators, filters, couplers, and modulators, including photonic crystals^{28,29} and metamaterials,³⁰ which has fueled the enormous success of photonics and microwave works. Similarly, manipulation of subwavelength surface plasmons by altering surfaces of 3D metals has been of significant interest in photonics.^{1–6} Our work reports a parallel development with ultra-subwavelength 2D plasmons for electronics.

■ ASSOCIATED CONTENT

● Supporting Information

Details on path splitting in plasmonic-electromagnetic interferometer; details on sample fabrication and measurement techniques including calibration and de-embedding of parasitic effects; circuit modeling; additional plasmonic crystal devices, and measurements. This material is available free of charge via the Internet at <http://pubs.acs.org>.

■ AUTHOR INFORMATION

Corresponding Author

*E-mail: donhee@seas.harvard.edu.

Notes

The authors declare no competing financial interest.

■ ACKNOWLEDGMENTS

The authors are grateful to the support of this research by the Air Force Office of Scientific Research under contract nos. FA 9550-09-1-0369 and FA 9550-08-1-0254. The circuit fabrication was performed at the Center for Nanoscale Science at Harvard University.

■ REFERENCES

- (1) Kitson, S. C.; Barnes, W. L.; Sambles, J. R. *Phys. Rev. Lett.* **1996**, *77*, 2670–2673.
- (2) Ebbesen, T. W.; Lezec, H. J.; Ghaemi, H. F.; Thio, T.; Wolff, P. A. *Nature* **1998**, *391*, 667–669.
- (3) Zia, R.; Brongersma, M. L. *Nat. Nanotechnol.* **2007**, *2*, 426–429.
- (4) Bozhevolnyi, S. I.; Erland, J.; Leosson, K.; Skovgaard, P. M. W.; Hvam, J. M. *Phys. Rev. Lett.* **2001**, *86*, 3008–3011.
- (5) Kocabas, A.; Seckin Senlik, S.; Aydinli, A. *Phys. Rev. B* **2008**, *77*, 195130.
- (6) Iwase, H.; Englund, D.; Vuckovic, J. *Opt. Express* **2008**, *16*, 426–434.
- (7) Barnes, W. L.; Dereux, A.; Ebbesen, T. W. *Nature* **2003**, *424*, 824–830.
- (8) Polman, A. *Science* **2008**, *322*, 868–869.
- (9) Gramotnev, D. K.; Bozhevolnyi, S. I. *Nat. Photonics* **2010**, *4*, 83–91.
- (10) Akimov, A. V.; Mukherjee, A.; Yu, C. L.; Chang, D. E.; Zibrov, A. S.; Hemmer, P. R.; Park, H.; Lukin, M. D. *Nature* **2007**, *450*, 402–406.
- (11) Oulton, R. F.; Sorger, V. J.; Zentgraf, T.; Ma, R.-M.; Gladden, C.; Dai, L.; Bartal, G.; Zhang, X. *Nature* **2009**, *461*, 629–632.
- (12) Economou, E. N. *Phys. Rev.* **1969**, *182*, 539–554.
- (13) Staffaroni, M.; Conway, J.; Vedantam, S.; Tang, J.; Yablonovitch, E. arXiv:1006.3126 2010.
- (14) Allen, S. J.; Tsui, D. C.; Logan, R. A. *Phys. Rev. Lett.* **1977**, *38*, 980–983.
- (15) Allen, S. J.; Störmer, H. L.; Hwang, J. C. M. *Phys. Rev. B* **1983**, *28*, 4875–4877.
- (16) Kukushkin, I. V.; Smet, J. H.; Mikhailov, S. A.; Kulakovskii, D. V.; von Klitzing, K.; Wegscheider, W. *Phys. Rev. Lett.* **2003**, *90*, 156801.
- (17) Burke, P. J.; Spielman, I. B.; Eisenstein, J. P.; Pfeiffer, L. N.; West, K. W. *Appl. Phys. Lett.* **2000**, *76*, 745–747.
- (18) Mackens, U.; Heitmann, D.; Prager, L.; Kotthaus, J. P.; Beinvogl, W. *Phys. Rev. Lett.* **1984**, *53*, 1485–1488.
- (19) Knap, W.; Lusakowski, J.; Parenty, T.; Bollaert, S.; Cappy, A.; Popov, V. V.; Shur, M. S. *Appl. Phys. Lett.* **2004**, *84*, 2331–2333.
- (20) Eguiluz, A.; Lee, T. K.; Quinn, J. J.; Chiu, K. W. *Phys. Rev. B* **1975**, *11*, 4989–4993.
- (21) Luryi, S. *Appl. Phys. Lett.* **1988**, *52*, 501–503.
- (22) Stern, F. *Phys. Rev. Lett.* **1967**, *18*, 546–548.
- (23) Allen, S. J., Jr.; Derosa, F.; Bhat, R.; Dolan, G.; Tu, C. W. *Phys. B + C* **1985**, *134*, 332–336.
- (24) Dyakonov, M.; Shur, M. *Phys. Rev. Lett.* **1993**, *71*, 2465–2468.
- (25) Nusinsky, I.; Hardy, A. A. *Phys. Rev. B* **2006**, *73*, 125104.
- (26) Sirtori, C. *Nature* **2002**, *417*, 132–133.
- (27) Ju, L.; Geng, B.; Horng, J.; Girit, C.; Martin, M.; Hao, Z.; Bechtel, H. A.; Liang, X.; Zettl, A.; Shen, Y. R.; Wang, F. *Nat. Nanotechnol.* **2011**, *6*, 630–634.
- (28) Yablonovitch, E. *Phys. Rev. Lett.* **1987**, *58*, 2059–2062.
- (29) John, S. *Phys. Rev. Lett.* **1987**, *58*, 2486–2489.
- (30) Smith, D. R.; Pendry, J. B.; Wiltshire, M. C. K. *Science* **2004**, *305*, 788–792.